Structural and spectroscopic characterization of a HdrA-like subunit from *Hyphomicrobium denitrificans*

Corvin Ernst[1], Kanwal Kayastha[2] (ID), Tobias Koch[1,*], Sofia S. Venceslau[3] (ID), Inês A. C. Pereira[3] (ID), Ulrike Demmer[2], Ulrich Ermler[2] and Christiane Dahl[1] (ID)

1 Institut für Mikrobiologie & Biotechnologie, Rheinische Friedrich-Wilhelms-Universität Bonn, Bonn, Germany
2 Max-Planck-Institut für Biophysik, Frankfurt, Germany
3 Instituto de Tecnologia Química e Biológica António Xavier, Universidade Nova de Lisboa, Oeiras, Portugal

Many bacteria and archaea employ a novel pathway of sulfur oxidation involving an enzyme complex that is related to the heterodisulfide reductase (Hdr or HdrABC) of methanogens. As a first step in the biochemical characterization of Hdr-like proteins from sulfur oxidizers (sHdr), we structurally analyzed the recombinant sHdrA protein from the Alphaproteobacterium *Hyphomicrobium denitrificans* at 1.4 Å resolution. The sHdrA core structure is similar to that of methanogenic HdrA (mHdrA) which binds the electron-bifurcating flavin adenine dinucleotide (FAD), the heart of the HdrABC-[NiFe]-hydrogenase catalyzed reaction. Each sHdrA homodimer carries two FADs and two [4Fe–4S] clusters being linked by electron conductivity. Redox titrations monitored by electron paramagnetic resonance and visible spectroscopy revealed a redox potential between −203 and −188 mV for the [4Fe–4S] center. The potentials for the FADH•/FADH⁻ and FAD/FADH• pairs reside between −174 and −156 mV and between −81 and −19 mV, respectively. The resulting stable semiquinone FADH• species already detectable in the visible and electron paramagnetic resonance spectra of the as-isolated state of sHdrA is incompatible with basic principles of flavin-based electron bifurcation such that the sHdr complex does not apply this new mode of energy coupling. The inverted one-electron FAD redox potentials of sHdr and mHdr are clearly reflected in the different FAD-polypeptide interactions. According to this finding and the assumption that the sHdr complex forms an asymmetric HdrAA′B1C1B2C2 hexamer, we tentatively propose a mechanism that links protein-bound sulfane oxidation to sulfite on HdrB1 with NAD⁺ reduction via lipoamide disulfide reduction on HdrB2. The FAD of HdrA thereby serves as an electron storage unit.

Database

Structural data are available in PDB database under the accession number 6TJR.

Abbreviations

DLHD, dihydrolipoamide dehydrogenase; Dsr, dissimilatory sulfite reductase; EPR, electron paramagnetic resonance; FAD, flavin adenine dinucleotide; FBEB, flavin-based electron bifurcation; Hdr, heterodisulfide reductase; LbpA, lipoate-binding protein; mHdr, Hdr system from methanogens; MOPS, 3-(*N*-morpholino)propanesulfonic acid; NAD, nicotinamide adenine dinucleotide; rms, root mean square; sHdr, heterodisulfide reductase-like system from sulfur oxidizers; SHE, standard hydrogen electrode; TrxR, thioredoxin reductase.

Introduction

Sulfur is a very versatile element and undergoes permanent biogeochemical cycling in terrestrial as well as in marine environments. Dissimilatory sulfate-reducing prokaryotes use sulfate as a respiratory electron acceptor instead of oxygen or nitrate [1]. On the other hand, hydrogen sulfide, elemental sulfur, and other reduced sulfur compounds serve as electron donors for a huge array of chemo- and photolithotrophic prokaryotes [2–9]. While a considerable portion of these organisms employs the comparatively well-characterized dissimilatory sulfite reductase (Dsr) pathway of sulfur oxidation [10,11], a novel pathway involving a new lipoate-binding protein (LbpA) and a heterodisulfide reductase (Hdr)-like complex resembling HdrABC from methanogens [12] has recently been identified in the Alphaproteobacterium *Hyphomicrobium denitrificans* by reverse genetics [13,14]. The relevant genes *hdrC1B1AhyphdrC2B2hyp-lbpA* also occur in a large number of other sulfur-oxidizing bacteria and archaea (e.g., species of the genera *Acidithiobacillus*, *Thioalkalivibrio*, *Aquifex*, *Sulfolobus* or *Metallosphaera*). Strong responses of these genes and the encoded proteins to the presence of reduced sulfur compounds have been reported in numerous transcriptomic and proteomic studies [3,14–18].

In the majority of methanogenic archaea, a cytoplasmic Hdr (HdrABC)–[NiFe]-hydrogenase (MvhAGD) complex reduces both the heterodisulfide of coenzyme M and coenzyme B (CoM–S–S–CoB) and ferredoxin by oxidizing two H_2 molecules in the terminal step of their energy metabolism [19–22]. This coupling of an exergonic and endergonic reduction mediated by a flavin is called flavin-based electron bifurcation (FBEB) [19]. The flavin in methanogenic Hdrs (mHdr) is a flavin adenine dinucleotide (FAD) bound to the mHdrA subunit [12]. mHdrA homologs are widely distributed in nonmethanogenic prokaryotes such as sulfur oxidizers, already mentioned, sulfate reducers, anaerobic methanotrophic archaea, or metal reducers [23–26]. It has been speculated that HdrA in these nonmethanogens may also have an electron-bifurcating function [27]. Besides the prosthetic group FAD, HdrA homologs contain one [4Fe–4S] cluster detectable by its characteristic C–X_{11-13}–C–X_3–CC signature motif [12]. In comparison with mHdrA, HdrA from sulfur oxidizers (sHdrA) lacks both the central and the carboxy-terminal ferredoxin domains each carrying two iron–sulfur clusters, and the N-terminal part, which binds one [4Fe–4S] cluster [14]. Thus, sHdrA is predicted to contain only one instead of the six [4Fe–4S] clusters embedded inside mHdrA.

Biochemical information on Hdr-like complexes from sulfur oxidizers is extremely scarce [13,14,28]. Co-purification of sHdrAB1B2C1C2 from membranes of the hyperthermophilic bacterium *Aquifex aeolicus* provided a first milestone, revealing the formation of a large protein complex consisting of several different sHdr subunits [28]. However, a functional role or enzymatic activity for this complex could not be assigned. We started filling this knowledge gap by determining the crystal structure of recombinant sHdrA from the model organism *H. denitrificans* and the redox potentials of the [4Fe–4S]-cluster and the FAD cofactor via electron paramagnetic resonance (EPR) and UV-visible spectroscopy. First insights are gained into the structure and possible catalytic processes performed by Hdr-like complexes of sulfur oxidizers.

Results

sHdrA is an iron–sulfur flavoprotein

Recombinant sHdrA from *H. denitrificans* carrying a Strep-tag at its carboxy-terminus was produced as a soluble protein in *Escherichia coli* BL21 Δ*iscR* [29] grown anaerobically on fumarate [30]. One liter *E. coli* culture routinely yielded 7–8 mg of pure protein [14]. 2.5–3.5 mol iron and sulfur per mol sHdrA monomer were determined for different preparations, fully in line with one [4Fe–4S] cluster predicted from the sequence. The protein displayed spectral properties typical for iron–sulfur flavoproteins.

Overall structure of sHdrA

The structure of sHdrA was determined at 1.4 Å resolution with R/R_{free} factors of 16.2%/19.1% (Table 1) by using the single anomalous dispersion method for phase determination. sHdrA adopts a thioredoxin reductase (TrxR) fold (Fig. 1) [31] composed of two classical dinucleotide-binding (Rossmann) domains as originally found for glutathione reductase [32]. The FAD-binding domain (2–115, 271–341) binds the flavin cofactor at the C-terminal end of the central β-sheet in the classical manner, the isoalloxazine ring being packed between the two domains (Fig. 1A). The [4Fe–4S] cluster-binding domain (116–270) has embedded the [4Fe–4S] cluster between the C-terminal end of the central β-sheet and the N-terminal side of α-helix 180 : 195. The edge-to-edge distance between two redox centers is 9.4 Å (Fig. 1A), which allows physiologically relevant electron transfer rates between them.

Table 1. Statistics of X-ray structure analysis.

Crystal	sHdrA	sHdrA (SAD data)
Crystallization		
Protein solution	20 mg·mL^{-1} sHdrA, 20 mM Tris/ HCl, pH 7.2, 50 μM FAD	
Crystallization conditions	0.1 M MES, pH 6.5 25% (w/v) PEP 629	
Cryo conditions	0.1 M MES, pH 6.5 35% (w/v) PEP 629	
Data collection		
Space group	P6$_5$	P6$_5$
Wavelength (Å)	1.0	1.739
Resolution (Å)	50.0–1.43 (1.48–1.43)	50.0–2.2
Unit cell *a, c* (Å)	145.6, 64.1	145.4, 64.1
Redundancy	5.8 (2.4)	14.0 (5.8)
Completeness (%)	96.70 (74.0)	94.9 (62.5)
R_{sym} (%)	4.5 (100.5)	5.6 (25.4)
$I/\sigma(I)$	20.1 (1.0)	35.5 (8.1)
$CC_{1/2}$	100 (40.3)	100 (96.3)
Refinement statistics		
Subunits per asym. unit	2	
No. atoms polypeptide, cofactors, solvent	5291, 206, 604	
$R_{working}$, R_{free} (%)	16.2 (34.5), 19.1 (34.6)	
$B_{average}$ (Å^2) polypeptide, ligands, solvent	25.4, 48.7, 33.9	
R.m.s. deviation		
Bond lengths (Å)	0.0155	
Bond angles (°)	1.63	
Ramachandran Plot		
Favored, outliers (%)	97.0, 0.59	

The nearest structurally known relative of sHdrA is mHdrA, the core subunit of the methanogenic Hdr complex (5odc) which binds FAD and the [4Fe–4S] cluster at equivalent positions [12]. Their overall rms (root mean square) deviation is 1.5 Å (337 of 653 residues, sequence identity 32%). In addition, sHdrA shares a high structural similarity to (low-molecular-mass) TrxR. The lowest rmsd of 3.4 Å (287 of 305; 23%) and 3.4 Å (287 of 303; 19%) were calculated for the *Thermoplasma acidophilum* (3cty) and *Lactococcus lactis* (5mh4) enzymes, respectively [33,34]. TrxR does

not contain a [4Fe–4S] cluster but instead binds NADP (Fig. 1B). An exception is the *T. acidophilum* enzyme [33] whose electron donor is unknown. For (low-molecular-mass) TrxR two structural forms are distinguished depending on the orientation of the FAD and [4Fe–4S] cluster (NADP) domains. In the first conformational state, FADH$^-$ is oxidized by hydride transfer to the adjacent disulfide, while in the second state FAD is reduced by NADPH [31,35]. sHdrA is present in the second state.

Just as mHdrA, *H. denitrificans* sHdrA is present as a homodimer characterized by an extended interface of 2470 Å^2 built up between the two FAD domains and between the two [4Fe–4S] cluster domains (Fig. 1A). In sHdrA, the edge-to-edge distances for the two isoalloxazine rings, the two [4Fe–4S] clusters, and the FAD and the [4Fe–4S] cluster of the counter subunits are 18.8, 11.5 and 17.8 Å, respectively. TrxR also oligomerizes to a homodimer, however, the two monomers are oriented differently compared to HdrA; their two-fold axes are rotated by 90° relative to each other (Fig. 1B). In TrxR, the interface is essentially formed by the FAD domains resulting in a smaller contact area of 1640 Å^2.

FAD- and [4Fe–4S]-cluster binding sites

Although the basic architecture of the FAD-binding site is shared by all members of the TrxR family [31], the conformation of the polypeptide segments and of relevant side chains contacting the isoalloxazine ring are substantially changed in HdrA proteins (Fig. 2). Most notable are an elongated segment following strand 26:33 and segment 131–141 linking the FAD- and [4Fe–4S] cluster-binding domains. In both sHdrA and mHdrA, the isoalloxazine is essentially buried inside the polypeptide scaffold, whereas especially in the second NADP-bound form of TrxR, the isoalloxazine is accessible from two sides. In sHdrA, the isoalloxazine is in a slightly bent conformation mainly provided by hydrophobic side chains such as Val183, Ile179, Ile322, Tyr45, Leu48, and Val49 pointing to the *si-* and *re*-faces (Fig. 2A,B). In mHdrA, FAD is not in a butterfly conformation.

The rather hydrophobic character but not individual residues of the isoalloxazine binding site are conserved between sHdrA and mHdrA (Fig. 2C). A hydrogen bond (Fig. 2A) is formed between the functionally important N5 and a water molecule, which is hydrogen-bonded to Lys47-O, Glu137-OE1 and via a second water molecule to Glu190-OE2. In mHdrA, however, N5 and O4 are hydrogen-bonded with Lys409-NZ anchored in its position by Glu356-OE2 (Fig. 2C). For
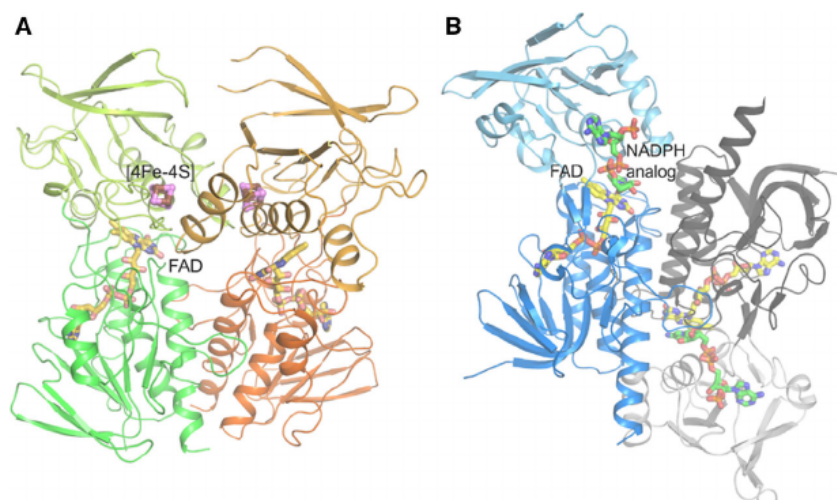
Fig. 1. Structure of sHdrA from *Hyphomicrobium denitrificans*. (A) sHdrA dimer and (B) TrxR dimer (Both produced with PYMOL). Both the FAD-binding domain (in green, orange in sHdrA, and in blue, gray in TrxR) and the [4Fe–4S] cluster domain (in lemon, lightorange, the equivalent NADPH domain of TrxR in lightblue, lightgray) are built up of a parallel six-stranded β-sheet flanked by three α-helices and a three-stranded β-meander. The edge-to-edge distance between the benzylmethyl of FAD (as stick model) and Fe1 of the [4Fe–4S] cluster (Fe as brown and S as magenta spheres) of sHdrA is 9.4 Å. The subunit arrangement and therefore also the subunit–subunit interfaces are different between HdrA and TrxR.

TrxR enzymes no direct N5-polypeptide interactions are reported but variable water-mediated hydrogen bonds to nonconserved polar residues (Fig. 2D). Hydrogen bonds invariant among TrxR family members are formed between O2 and Ile322-NH positioned at the N-terminal end of helix 322 : 340 and between the N3-C4 = O4 groups and main chain peptide nitrogen and carbonyl groups or asparagine side chains (Fig. 2). A notable difference is a further water-mediated hydrogen bond between O2 and Asp323 in sHdrA and between O2 and Lys524' in mHdrA (Fig. 2A–C). Lys524' points from the counter mHdrA (marked by an apostrophe) toward the isoalloxazine ring, which is enabled by the different conformation of the elongated segment following strand 26:32 of sHdrA compared to mHdrA.

The [4Fe–4S] cluster-binding is well conserved in sHdrA and mHdrA. The four irons are coordinated with Cys163, Cys176, Cys180, and Cys181 (sHdrA numbering) and all sulfurs interact with at least one proton donor (Fig. 3). Arg167, Arg208, and the partially positively charged N-terminal end of helices 180 : 195 and 212' : 225' create a positively charged [4Fe–4S] cluster binding pocket.

UV-vis spectroscopical characterization

Just as expected for a protein carrying FADs and iron–sulfur clusters in a 1 : 1 ratio, the UV-vis spectrum for sHdrA in the 'as-isolated' state is dominated by the absorption of FAD. This was apparent in spectra taken at pH 8.0 by absorption maxima at 360 and 455 nm with shoulders at 433 and 485 nm (Fig. 4A). A broad absorption band observed at 590–650 nm in the *H. denitrificans* sHdrA spectra is a characteristic feature for a stable FAD semiquinone radical in a neutral state (FADH•) [36–38]. The relatively pronounced absorption at 360 nm indicated that a part of the FAD semiquinone population was present in the anionic (FAD•⁻) state at pH 8.0. By shifting the pH to 7.0, the absorbance at 590–650 nm further increased, while the band at 360 nm decreased simultaneously (Fig. 4B). This finding corresponds exactly to the type of behavior expected. The equilibrium is shifted from a partially anionic FAD•⁻ toward a neutral FADH• state upon protonation [38]. Under the crystallization conditions at pH 6.5, the FAD of sHdrA is presumably present in a partial neutral semi-reduced state.

Further evidence for the presence of a stable FADH• in sHdrA was obtained by stepwise oxidation of 50 μM prereduced protein with potassium ferricyanide ($E^{0\prime}$ = +0.452 V in 0.2 M Tris/HCl, pH 7.0, [39]; Fig. 4C). Reduced sHdrA exhibited low absorption at 610 nm (Fig. 4C, dark blue spectrum), while the absorption value increased by gradual oxidation of the protein (Fig. 4C, blue to green spectra). A maximum was reached after addition of an equimolar amount of ferricyanide (50 μM) when one electron is withdrawn from each reduced FAD cofactor. Upon further oxidation, absorption at 610 nm decreased
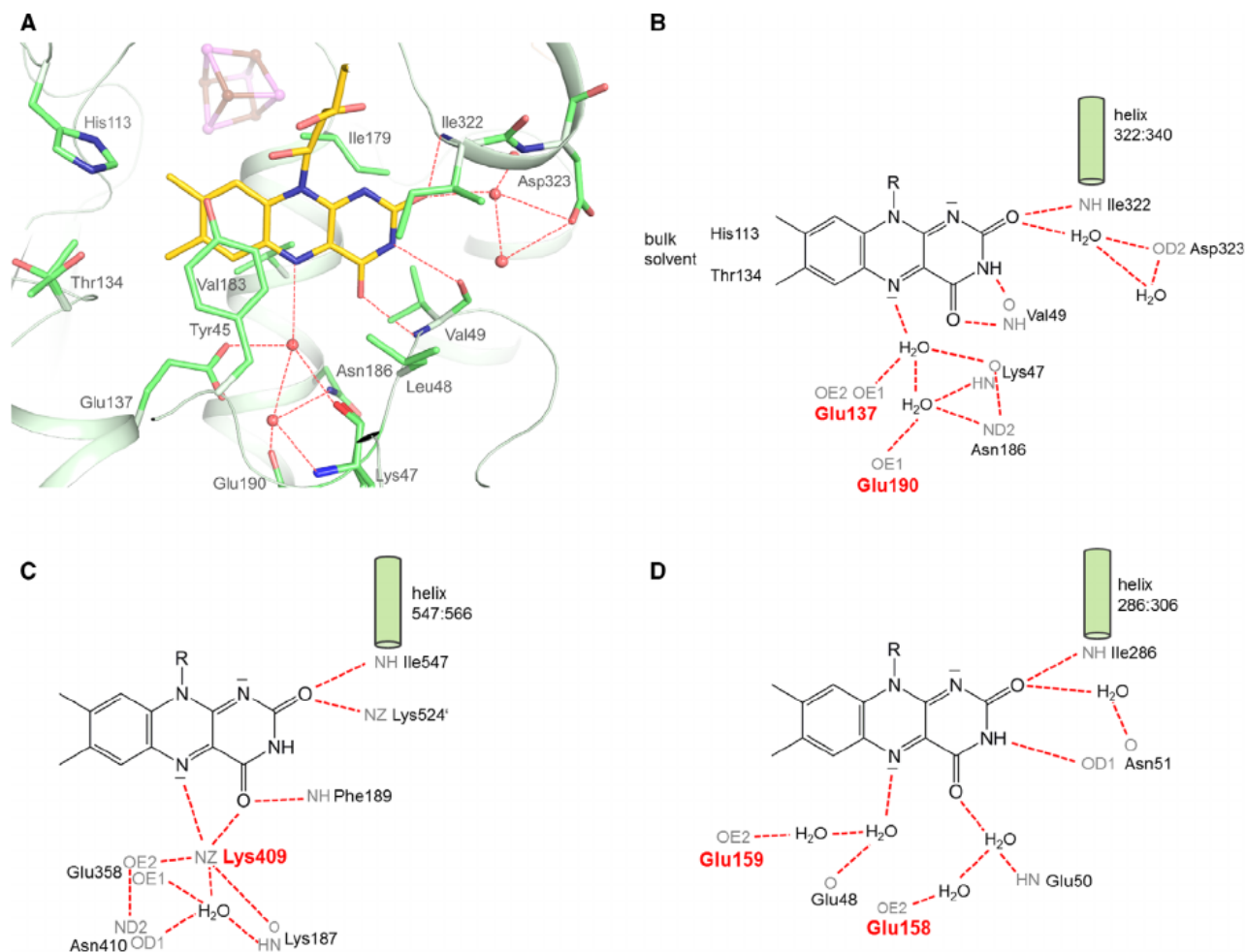
Fig. 2. FAD-binding sites. (A) Structure (drawn with PYMOL) and (B) scheme of the sHdrA. The isoalloxazine ring (carbon in yellow) of sHdrA (carbon in green) and the mHdrA are encapsulated in comparison with that of TrxR thereby using a segment constructing the [4Fe–4S] cluster binding sites, the short domain linker helix 133 : 142 and the counter HdrA monomer of the homodimer. Scheme of the isoalloxazine surrounding of sHdrA (B), of mHdrA (C), and of TrxR of *L. lactis* (D). Hydrogen bonds are drawn as red dashed lines. N5 of sHdrA and TrxR is contacted by hydrogen acceptors preferably stabilizing FADH⁻ and FADH• whereas N5 of mHdrA is hydrogen-bonded with Lys409 stabilizing the oxidized FAD.

again. After its disappearance, the FAD of sHdrA is completely oxidized accompanied with a strong increase of absorption at 456 nm. Corresponding results were obtained by titration in the reverse direction, that is, by stepwise reduction of pre-oxidized sHdrA with titanium citrate ($E^{0\prime} = -0.48$ mV at pH 7.0 [40]; Fig. 4D).

Potentiometric titration of FAD

In general, flavins can have a wide range of redox potentials (E_m, +150 to −500 mV [41]) and these are not predictable from the primary structure of the protein. The reduction potential of the sHdrA flavin was determined by a redox titration monitored by recording

UV/vis spectra. As-isolated sHdrA (50 μM) was titrated stepwise with sodium dithionite, which has a redox potential below −550 mV [42], and allows complete reduction of the flavin cofactor of the protein. Complete oxidation was achieved in a separate measurement by stepwise addition of 2,6-dichloroindophenol ($E^0 = +330$ mV at pH 6.0 [43]) as oxidant. This experiment allowed the assignment of the redox potentials of the FAD cofactor (Fig. 5). The ratio of oxidized/reduced FAD species was calculated from the UV-visible spectra at 456 nm and 610 nm, respectively, and plotted against the observed potential (Fig. 5A). A stable FADH• species appeared between −104 to −70 mV recognizable by a plateau in the titration curve at 456 nm. The FAD absorption at 590–650 nm was
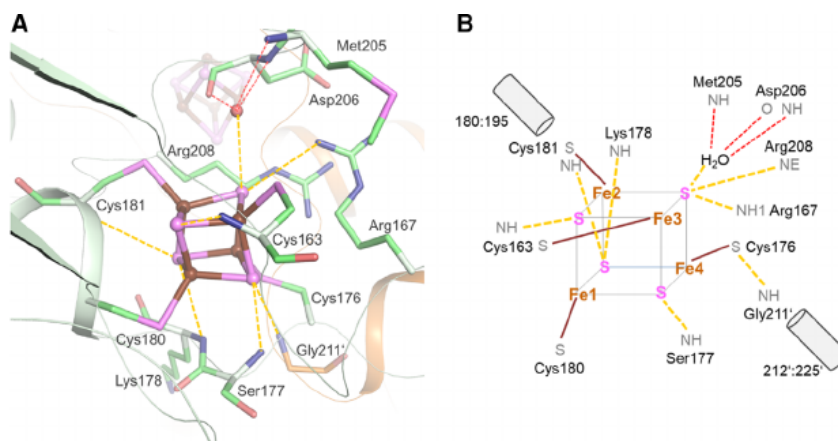
Fig. 3. [4Fe–4S] cluster binding site of sHdrA. (A) Structure (drawn with PYMOL) and (B) scheme of the polypeptide-[4Fe–4S] cluster interactions. The [4Fe–4S] cluster (Fe in brown, S in magenta) in sHdrA and the NADPH in TrxR occupy an identical position. The [4Fe–4S] cluster is encapsulated by the loop between strand 199 : 204 and helix 212′ : 225′ of both subunits (green, orange) and is primarily contacted by hydrogen bond donating groups and positively charged side chains. The interactions are shown as golden dashes.

highest at −104 mV and decreased again upon further reduction or oxidation, respectively (Fig. 5A). Titration curves can be explained by the Nernst equation

$$E = E° + 2.303(RT/nF)\log_{10}(c_{ox}/c_{red}) \qquad (1)$$

where E is the observed potential. When E is plotted against the logarithm of the concentration ratio of oxidized (c_{ox}) and the reduced species (c_{red}), linear functions can be derived from the data and statistically analyzed (Fig. 5B–E). $E°'$ is taken from the plots at $c_{ox} = c_{red}$, and 59 divided by the slope gives n, the number of electrons involved in the reaction. Redox potentials were determined by following the absorbance at 456 and 610 nm. The calculations at 610 nm are, however, based on the predominant presence of the flavin in the FADH• state at around −100 mV which makes them less reliable.

The values of the midpoint potential calculated for the FADH•/FADH⁻ couple were $E°' = −168 ± 5$ mV (Fig. 5B) and −160 ± 4 mV (Fig. 5C), respectively. In both cases, data fitted well to the Nernst equation ($R^2 = 0.95$ and 0.97, respectively) and indicated a one-electron transition ($n = 0.97 ± 0.07$ for 456 nm and $n = 0.99 ± 0.06$ for 610 nm). When holding n fixed to 1, the potentials amount to −169 ± 5 mV ($R^2 = 0.95$) and −160 ± 4 mV ($R^2 = 0.97$), respectively (Fig. 5A–C).

The analysis of the FAD/FADH• couple is not as unambiguous as that for FADH•/FADH. The data obtained at 456 nm for the FAD/FADH• couple yielded $E°' = −24 ± 4$ mV and $n = 2.25 ± 0.30$ (Fig. 5 D). The data points could not be fitted with a one-

electron but with a two-electron Nernst equation shown in Fig. 5D and in the upper part of Fig. 5A. For $n = 2$, the midpoint potential was −23 ± 4 mV ($R^2 = 0.86$). At 610 nm the fit of the titration points with the Nernst equation was comparably poor ($R^2 = 0.44$) and gave $E°' = −59 ± 10$ mV and $n = 1.58 ± 0.70$ for the numbers of electrons involved (Fig. 5E). Since only an integer number of electrons can be transmitted, the titration curve was simulated for $n = 1$ and $n = 2$ resulting in midpoint potentials of −70 ± 11 mV ($R^2 = 0.29$) and −54 ± 10 mV ($R^2 = 0.41$). The reason for the shape of the FAD/FADH• titration curve that rather reflects, in particular at 456 nm, a two-electron transition and the origin of a potential second electron remains obscure at this point. Nevertheless, the stable FADH• peak around −100 mV at 456 and 610 nm, respectively, and its increase/decrease upon further oxidation indicates that definitely one electron stems from FADH• (Fig. 5A).

In summary, the presented visible titration data are in accordance with the formation of a stable FADH• species and indicating two temporally separated one-electron steps for the FAD/FADH⁻ transition. Although very good agreement was obtained for the midpoint potential of the FADH•/FADH⁻ couple at both wavelengths analyzed, some uncertainty remains regarding the value for the FAD/FADH• pair, albeit it is clearly more positive. More accurate determination of the actual potentials will have to await determination of the spin concentration of the FADH• radical as has been outlined for iron–sulfur clusters by others [44].
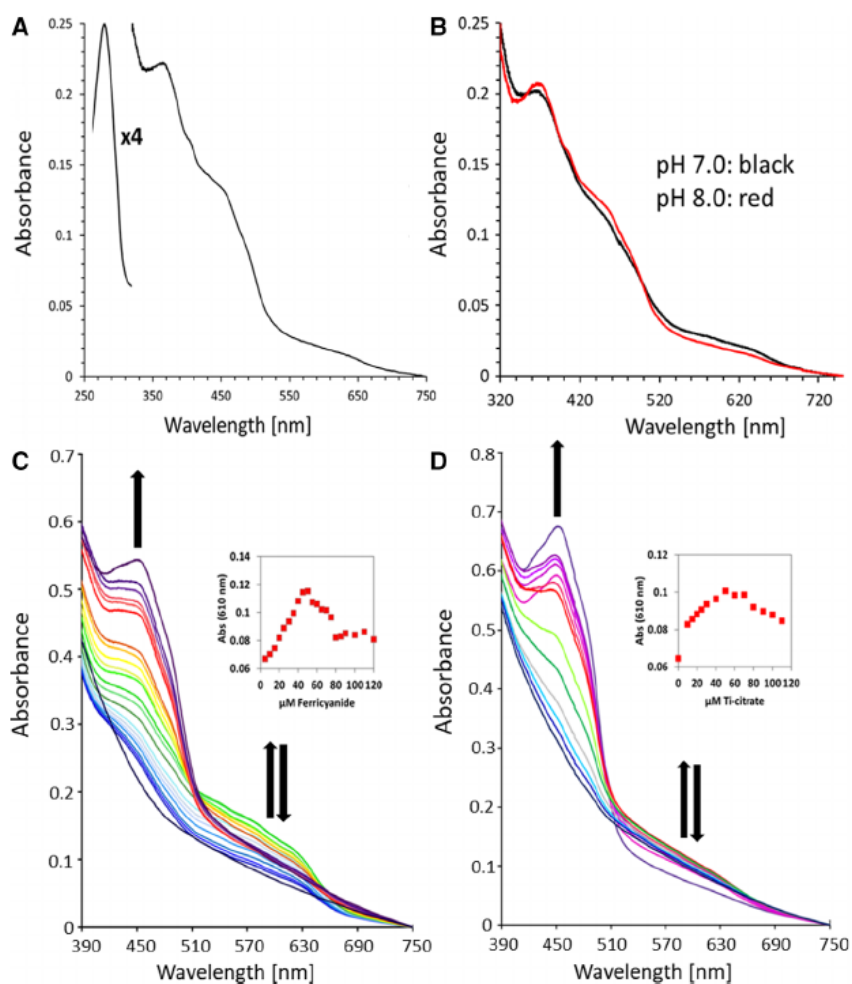
Fig. 4. UV-vis spectroscopic characterization of sHdrA (A) UV-vis spectrum of 18 μM *Hyphomicrobium denitrificans* sHdrA in 200 mM Tris/HCl, pH 8.0 in the as-isolated state. (B) Comparison of spectra taken at pH 7.0 and pH 8.0. (C) Oxidation of prereduced sHdrA (50 μM) by stepwise addition of ferricyanide as oxidant. Formation of a stable, singly reduced FADH• is observed as a broad absorption centered around 610 nm. The semiquinone intermediate shows the highest absorption at 610 nm (green curves). The absorbance at 610 nm decreases as the protein-bound FAD becomes oxidized (purple curves) or reduced (FADH⁻, blue curves), respectively. Arrows show direction of absorbance changes. Insets show changes in the FADH• amount at A_{610} as a function of oxidant. (D) Reduction of pre-oxidized sHdrA (50 μM, violet curve) by stepwise addition of titanium (III) citrate as reductant. Singly reduced FADH• is observed as a broad absorption centered around 610 nm (green curves). The absorbance at 610 nm decreases as the protein-bound FAD becomes oxidized (FAD, purple curves) or reduced (FADH⁻, blue curves), respectively. Arrows show direction of absorbance changes. Insets show changes in FADH• at A_{610} as a function of oxidant.

The X-band EPR spectrum of the as-purified sHdrA exhibited a typical broad signal centered at $g = 2.002$ characteristic of a flavin radical, that is, a one-electron-reduced FADH• (Fig. 6A) fully in line with UV-vis spectroscopic detection of this species.

Potentiometric titration of the [4Fe–4S] cluster

A redox titration of sHdrA using sodium dithionite as reductant was performed inside the anaerobic chamber, and followed by EPR to further characterize the [4Fe–4S] center of sHdrA (Fig. 6B,C). The flavin radical signal is masked by the presence of redox mediators and is not titratable by EPR. In the EPR spectrum of fully reduced HdrA a rhombic signal with $g_{max} = 2.053$, $g_{med} = 1.961$, and $g_{min} = 1.926$ is observed (Fig. 6B), which is characteristic for a single [4Fe–4S] center in agreement with the primary sequence and crystal structure data. The height of the g_{max} or g_{med} of the rhombic signal was followed during the titration (Fig. 6B) in order to determine the redox

potential of the center. Both g values gave rise to the same midpoint redox potentials within experimental error, namely approximately −197 mV (g_{max}) and −192 (g_{med}), and fit a one-electron process (Fig. 6C).

Discussion

Properties and function of sHdrA

The performed structural and spectroscopic characterization of sHdrA indicated substantial functional differences to those TrxR family members acting as hydride-transferring enzymes but also to mHdrA operating as a FBEB module. (a) HdrA and TrxR differ in their monomer–monomer arrangement. In HdrA, the side-by-side attachment of the FAD and [4Fe–4S] domains hold the two monomers together and shields both cofactors from one side (Fig. 1). In addition, the distance between the two [4Fe–4S] clusters is sufficiently short for a rapid electron transfer [45] (Fig. 2) thereby forming an electron-conducting and -storing
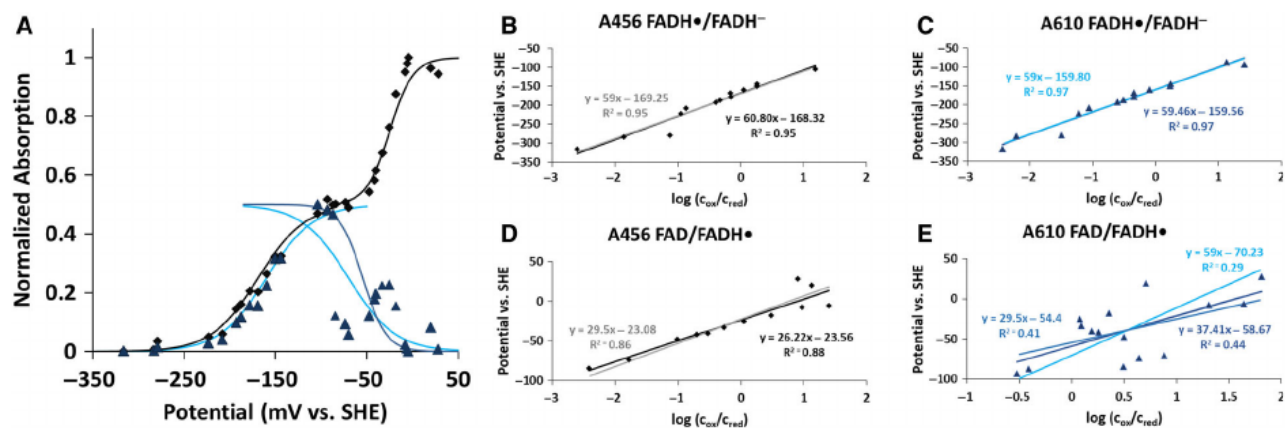
Fig. 5. Redox titration of sHdrA from *Hyphomicrobium denitrificans* followed by UV-visible spectroscopy. (A) Normalized absorbance versus potential plot for sHdrA at 456 nm (black diamonds) and 610 nm (blue triangles). Symbols represent experimental data. Solid lines are fitted curves. At 456 nm, there is the largest overall change in flavin absorbance between fully oxidized (FAD) and fully reduced (FADH⁻) forms. At 610 nm, the FADH• absorbance is near maximal and the data show the formation and the decay of this species. Panels (B–E) show Nernst plots linearized by plotting the observed potentials against the logarithm of the ratio of the concentration of oxidized (c_{ox}) and reduced species (c_{red}; black and dark blue lines, for 456 and 610 nm, respectively). Equations for regression lines are given as insets (printed in black and dark blue) and provided first approximations for the redox potentials and number of electrons (*n*) transferred as outlined in the Results section. As only integer numbers of electrons can be transmitted in the actual reactions, those linear equations were also derived that yielded the highest coefficients of determination with slopes fixed to values corresponding to one or two electrons (Fig. 5B–E, lines and equations printed in gray, light blue, and turquoise). Based on these analyses, the titration of the FADH•/FADH⁻ couple was now fitted with a one-electron Nernst equation and curves with $E^{0\prime}$- values of −169 mV for 456 nm and −160 mV for 610 nm were added to Fig. 5A (black line from −350 to −104 mV and turquoise line starting at −350 mV). The FAD/FADH• couple at 456 nm was fitted with a two-electron Nernst curve (black line, −104 to +28 mV) with an $E^{0\prime}$ value of −23 mV, while the data at 610 nm were fitted for a one-electron transition with an $E^{0\prime}$ value of −70 mV (turquoise line ending at 50 mV) and a two-electron transition with an $E^{0\prime}$ value of −54 mV (light blue line ending at 50 mV; Fig. 5A).

unit between the two FAD and the two [4Fe–S] clusters. In contrast, the TrxR dimer interface only consists of two FAD domains (Fig. 1B) and thus enables a 66° rotation of the NADP domain to cycle between FAD-reducing and -oxidizing forms [35]. (b) In contrast to TrxR, the isoalloxazine ring of the HdrAs is buried inside the protein implicating no access for an external hydride-transferring compound. (c) The NADP binding site in TrxR is converted into a [4Fe–S] cluster binding site in HdrAs, predominantly by prolonging helix 180 : 195 by one turn and by redesigning its preceding loop (Fig. 3). (d) sHdrA cannot operate as FBEB enzyme as on one hand the ferredoxin insertion/extension domains essential for bifurcation in mHdrA are lacking in sHdrA [12]. On the other hand, the redox properties of FAD in sHdrA ($E^{0\prime}_{FAD/FADH\bullet} > E^{0\prime}_{FADH\bullet/FADH}-$) indicate a stable FADH• semiquinone (Figs 5 and 6), which is incompatible with the current concept of FBEB. This mode of energy coupling requires an unstable, energy-rich semiquinone with inverse redox properties ($E^{0\prime}_{FAD/FADH\bullet} \ll E^{0\prime}_{FADH\bullet/FADH}-$) to donate an electron to the low-potential electron donor ferredoxin [27,46]. Recently, an unstable semiquinone with a half-life of

only 10 ps was observed for the FBEB enzyme NADH-dependent ferredoxin-NADP⁺ oxidoreductase [47]. The described different polypeptide environment of the N5 and the N2–C1=O1 groups in sHdrA and mHdrA is in line with the determined inverted redox potentials. (e) The determined midpoint reduction potential of −203 to −188 mV of the [4Fe–S] cluster is relatively high. Values for [4Fe–S]⁺/²⁺ clusters are mostly below −300 mV [48–50] and those for TrxR from *T. acidophilum* and *E. coli* are −305 mV (at pH 7, 30 °C) and −243 mV (at pH 7, 12 °C and in a disulfidic state of TrxR) [51,52], respectively. The [4Fe–S] cluster of sHdrA is located inside a pocket characterized by a positive electrostatic surface potential, which preferentially stabilizes the reduced [2 Fe²⁺, 2 Fe²·⁵⁺] state and thus explains the high redox potential. The redox potential of the FAD/FADH• and FADH•/FADH⁻ pairs is also relatively high in sHdrA probably due to the stabilization of protonated relative to an unprotonated N5 (Fig. 2B). The redox potential of the persulfide/sulfite pair is unknown but should be lower than or similar to that of the proposed terminal electron acceptor nicotinamide adenine dinucleotide (NAD⁺; $E^{0\prime} = −320 \pm 50$ mV). (6) The different redox
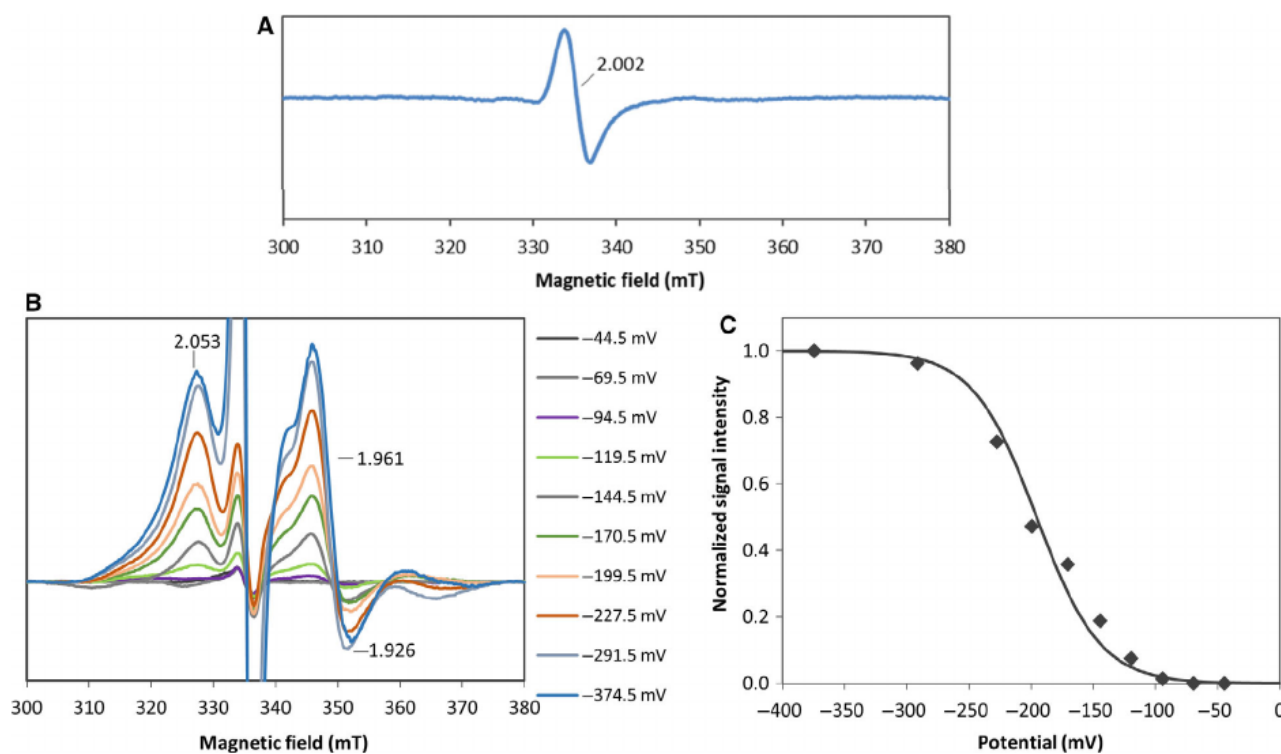
Fig. 6. EPR spectra of the as-isolated *Hyphomicrobium denitrificans* sHdrA. (A, B) EPR spectra taken during the redox titration and (C) Redox titration curve following the *g* value of 2.05. Linearization of the plot and statistical analysis were performed as described for the absorbance data in the visible range (Fig. 5). Best simulation of the experimental data (black diamonds) was achieved by assuming reduction of one Fe–S center ($n = 0.96 \pm 0.09$, $R^2 = 0.96$) with an $E^{0\prime}$ of −197 mV. Data acquired at the *g* value of 1.926 yielded comparable results ($E^0 = -192$ mV, $n = 0.92 \pm 0.07$, $R^2 = 0.98$) and are not shown here. Temperature of 5 K for all spectra except for spectra in A (18 K).

potentials between the [4Fe–4S] cluster and FAD may provide a first hint about the direction of the electron flow, even if their distances and redox potentials are shifted to a certain extent in the *in vivo* complex relative to the determined values of recombinant sHdrA. Accordingly, single electrons enter sHdrA via its single [4Fe–4S]-cluster, flow to FAD and exit sHdrA, which is the inverse direction as reported for mHdrA.

The Hdr complex of sulfur oxidizers (sHdr)

The genes encoding sHdrA, sHdrB1, sHdrB2, sHdrC1 and sHdrC2 are equivalently arranged in the same operon in all sulfur-oxidizing microorganisms containing *shdr* genes [8,11,13,14]. Based on the heterohexameric architecture of the recently reported methanogenic Hdr(ABC)$_2$ complex [12], the postulation of an asymmetric sHdr(AA′B$_1$B$_2$C$_1$C$_2$) complex appears to be plausible (Fig. 7). For model building, the structures of the individual subunits were calculated with the SwissModel server [53] and inserted into the mHdr hexamer instead of the corresponding mHdr subunits

(Fig. 7). The HdrA-HdrC and HdrB-HdrC interfaces are highly similar between the sulfur-oxidizing and methanogenic Hdr hexamers supporting the reliability of the model. In addition, the predicted asymmetric sHdr(AA′B$_1$B$_2$C$_1$C$_2$) complex coincides with the reported subunit composition of the purified sHdr complex from *A. aeolicus* [28]. Its molecular mass of 240 kDa derived from a Blue native gel [28] is similar to 225.3 kDa calculated for the *H. denitrificans* heterohexamer on the basis of the genome sequence.

The assumed hexameric sHdr architecture assigns sHdrC1/C2, as mHdrC, a function as redox relay between sHdrA and sHdrB1/B2. Like mHdrC, sHdrC1/C2 each contain two [4Fe–4S] clusters deduced from eight strictly conserved cysteines. The peripheral sHdrB1/B2 subunits are attributed a function as catalytic subunits like mHdrB. For CoM–S--S–CoB reduction mHdrB remarkably uses two unique noncubane [4Fe–4S] clusters both spectroscopically and structurally analyzed [54]. The nonmethanogen *H. denitrificans* lacks the classical CoM–S–S–CoB heterodisulfide and sHdrB1/B2 must possess other

enzymatic activities. sHdrB2 can be reliably assigned as a disulfide reductase due to the conservation of all 10 cysteines ligating the two noncubane [4Fe–4S] clusters in mHdrB [12,14]. In each cluster, four cysteines ligate the four iron atoms and a fifth provides the bridging sulfur of a [3Fe–4S] subcluster. The specific substrate of sHdrB2 remains, however, unknown. The model of sHdrB2 suggests an increase in the size of the substrate binding pocket compared with mHdrB because the loop prior to helix 223 : 236 is shortened in sHdrB2. The functional annotation of sHdrB1 is even more complicated because of significant sequence deviations from the classical active site noncubane iron–sulfur cluster-binding motif of mHdrB [14]. Four of the five cysteines in the
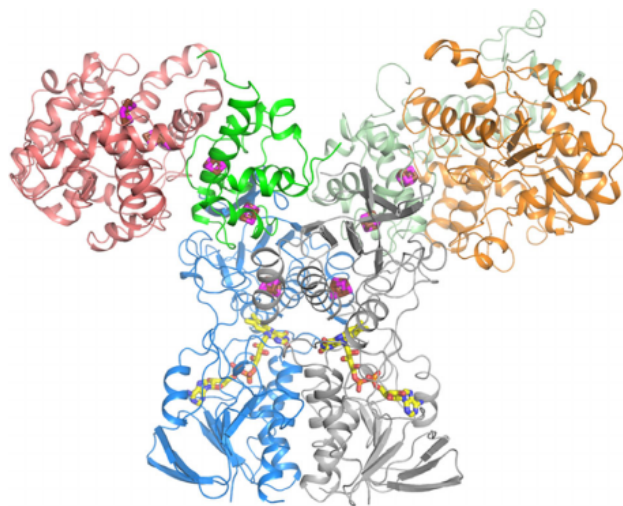
proximal iron–sulfur cluster of mHdrB [12] are present in sHdrB1 and the fifth is replaced by an aspartate, a residue known as iron ligand [55,56]. Three of the five cysteines ligating the second, distal noncubane iron–sulfur cluster in mHdrB [12] are conserved in sHdrB1 and two of them (Cys-41 and Cys-81 in mHdrB) are replaced by serine, a residue with reported iron-ligating capacity [57]. Therefore, sHdrB1 may also contain one or two functional Fe/S clusters, albeit not necessarily noncubane [4Fe–4S] clusters. The function of the sHdrC1-sHdrB1 branch and the concrete substrate is unknown, however, no participation in the catalytic process is unlikely. Notably, the binding pocket for CoM-SH is significantly reduced in size in sHdrB1 compared to mHdrB. No information is available about the binding of a redox protein to sHdrA in a suitable electron transfer distance to FAD. Therefore, the postulated catalytic mechanism (see below) does not consider FAD as electron relay.

The reaction of the sHdr complex

The sHdr pathway runs in the cytoplasm of sulfur-oxidizing prokaryotes where reduced sulfur is never processed in a free form, but rather in a protein-bound persulfidic form [11,58]. The sulfur ultimately stems from an oxidized inorganic sulfur substrate; for example, thiosulfate in the case of *H. denitrificans* and is delivered to the sHdr complex in the form of a protein persulfide via a cascade of sulfur transfer reactions [11,58]. The sHdr complex catalyzes the oxidation of the protein-bound sulfane sulfur to sulfite, the most likely end product [14]. The four released electrons are possibly shuttled to an oxidized lipoamide bound to the sHdr-specific LbpA [13] and the formed dihydrolipoamide is regenerated for the next reaction cycle by NAD^+-reducing dihydrolipoamide dehydrogenase (DLDH).

The limited data basis allows several preliminary mechanistic proposals. We will, however, only present one scenario in more detail that is compatible with the currently available data (Fig. 8). Accordingly, the formation of sulfite (SO_3^{2-}) from a protein-bound sulfane sulfur, R_1–CysS–S$^-$ is completely executed at the sHdrB1 active site. The sulfane sulfur and the cysteine sulfur may each be bound to an iron of the two postulated iron–sulfur centers of sHdrB1. Subsequently, the Fe-ligated sulfane sulfur is oxidized to the Fe-ligated sulfenate (–S–OH) and/or sulfinate ($-S-O_2^-$) intermediates *en route* to sulfite, reminiscent of the reactions on the siroheme iron [59]. Then, the released electrons could flow from sHdrB1 to

Fig. 7. Model of the sulfur-oxidizing Hdr-like complex (sHdrAA'B1C1B2C2). For model building of the sHdr hexamer, the structures of sHdrA (gray), sHdrA' (blue), sHdrC1 (lime), sHdrB1 (orange), sHdrC2 (green), and sHdrB2 (salmon) subunits were calculated by the SwissProt server based on the template of the mHdrBC. The sequence identities between sHdrC1(C2) and mHdrC are 18.7 (34.7) %, and between sHdrB1(B2) and mHdrB 21.5 (32.4) %. Subsequently, the mHdrA, mHdrB, and mHdrC subunits were exchanged by the corresponding sHdr subunits to obtain the structural model of the sHdr hexamer. The sHdrA-sHdrC and mHdrA-mHdrC interfaces are highly similar and do not involve the ferredoxin insertion/extension domains of mHdrA truncated in sHdrA as contact area [12]. Except for the differences in the sequence, sHdrB1 contains a prolonged N- and C-terminal extensions of ca. 100 and 50 residues compared to mHdrB and sHdrB2. While sHdrC1 was confidently modeled with mHdrC as template, the modeling of sHdrC2 for the last 70 amino acids failed. The terminal 70 residues are adjacent to the active site of sHdrB and might be crucial for substrate binding and specificity. We assume that sHdrC2 and sHdrB2 form one branch due to their closer relationship to mHdrB. The figure was generated with PYMOL.

sHdrB2 via the two [4Fe–4S] clusters of the sHdrA dimer which conducts electrons between the two sHdrBC branches. The two reduced noncubane [4Fe–4S] clusters of sHdrB2 would reduce oxidized lipoamide disulfide analogous to those of mHdrB that reduce the CoM–S–S–CoB heterodisulfide [12]. Dihydrolipoamide is finally reoxidized by NAD^+ reduction. In this mechanism, the two flavins have only a function as an electron sink in order to partly accept the four electrons rapidly released from the sulfur during oxidation at HdrB1 (Fig. 8). As pointed out, other mechanisms cannot be excluded yet. For example, the oxidation of the protein-bound sulfane sulfur to sulfite may not occur at one active site as described (Fig. 8) but instead in a concerted fashion at the active sites of sHdrB1 and sHdrB2. Further experiments, in particular, with the entire sHdr complex are required to shed light on the structure of the Fe/S clusters and on the mode of action of the sHdr complex.

Materials and methods

Production of recombinant sHdrA

The *H. denitrificans hdrA* gene with an additional carboxy-terminal Strep-tag encoding sequence was cloned in plasmid pET22b and overexpressed in *E. coli* BL21 (DE3) Δ*iscR*. One liter batches of lysogeny broth medium containing 100 mM 3-(*N*-morpholino)propanesulfonic acid (MOPS) buffer pH 7.4, 25 mM glucose and 2 mM iron ammonium citrate as well as ampicillin and kanamycin were inoculated with 5% (v/v) *E. coli* precultures hosting plasmid pET-22bHdhdrA [14] and cultivated in 2-L flasks at 37 °C and 180 r.p.m. until an OD600 of 0.4–0.6 was reached. Cultures were then moved into an anaerobic chamber (Coy Laboratory Products, Grass Lake, MI, USA) containing 98% N_2 and 2% H_2. Cysteine (0.5 mM), sodium fumarate (25 mM) and IPTG (0.1 mM) were added. Cultures were then transferred into completely filled and tightly closed 500 mL bottles, incubated for 48–72 h at 16 °C and harvested by centrifugation (11 000 *g*, 12 min). Cells were lysed by sonication in the anaerobic chamber. After removal of insoluble cell material by centrifugation (16 100 *g* for 30 min at 4 °C) protein was purified under strictly anaerobic conditions by Strep-Tactin affinity chromatography according to the manufacturer's instructions (IBA Lifesciences, Göttingen, Germany) followed by concentration to a final volume of < 2 mL via Amicon Ultracel-10K filters (Merck Millipore, Tullagreen, Ireland). The protein was stored under anaerobic conditions at −70 °C. One liter *E. coli* culture routinely yielded 7–8 mg of sHdrA. Purity was assessed by sodium dodecyl sulfate–polyacrylamide gel electrophoresis.
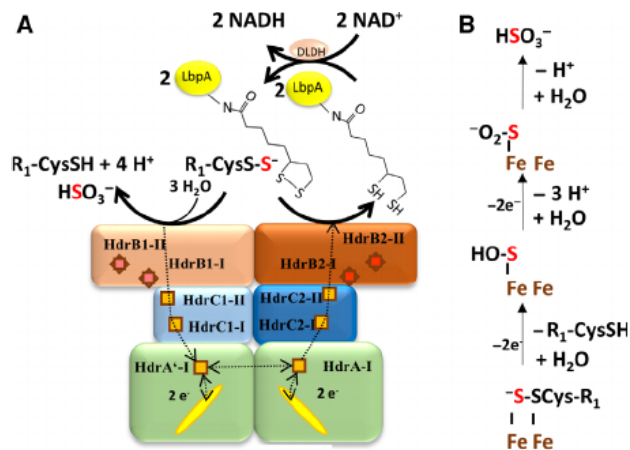

Fig. 8. Mechanistic scheme of the sulfur-oxidizing Hdr-like complex (sHdrAA'B1B2C1C2) reaction. (A) The proposed scenario of the reaction from a cysteine-bound persulfide (R_1–CysS–S^-) to sulfite is based on the assumption that sHdrB2 performs a disulfide/thiolate redox reaction, sHdrB1 acts as redox carrier/active site and sHdrA as redox carrier/storage unit but not as hydride donor for a disulfide-containing molecule or NADH. The sHdrB1/B2, HdrC1/C2, and HdrA subunits are depicted in orange, blue, and green, respectively. The following prosthetic groups are indicated: orange boxes, [4Fe–4S] clusters; dark red diamonds, noncubane iron-sulfur clusters; light red diamonds, iron–sulfur clusters of unclear nature; and yellow oval, FAD. Thiol groups and persulfides are shown in the protonated or ionized state according to their supposed pK_a values of around 8.5 [73] and 6.2 [74], respectively. Due to high reactivity, measuring the pK_a for a sulfenic acid is complicated and, as far as we are aware, estimated in a range of 6–10 or a value of 7.6 ± 0.3 for cysteine sulfenic acid [75,76]. The sulfinic acid functional group has a pK_a value at around 2 and is always deprotonated under physiological conditions [77]. We assume that R_1 is a sulfur carrier protein encoded in the *shdr* gene cluster or in its immediate environment, that is, TusA or DsrE [14]. The depicted scenario suggests that the sulfane sulfur is completely oxidized at the postulated iron–sulfur cluster(s) of HdrB1 yielding sulfite and a regenerated sulfur carrier protein R_1-CysSH. Four electrons flow via the [4Fe–4S] cluster of sHdrA to HdrB2 on which lipoamide disulfide may be reduced and regenerated by NAD^+ reduction catalyzed by DLDH. (B) Here, the details of the four-electron oxidation at the iron–sulfur clusters of sHdrB1 are outlined. The electrons are conducted away via the ligating irons.

Quantification of iron and sulfur

Quantification of non-heme iron and acid-labile sulfur was conducted as described by Fish [60] and King and Morris [61], respectively.

UV-visible titration of sHdrA

UV-visible absorbance spectroscopy was carried out at 20 °C on a Specord 210 UV/Vis-spectrophotometer (Analytik Jena, Jena, Germany). The protein sample (50 μM) was prepared in

500 µL of 200 mM ammonium acetate buffer (pH 6.0) and assembled in a quartz glass cuvette (Hellma Analytics, Müllheim, Germany) in the Coy anaerobic chamber. The cuvette was sealed with airtight septa, and titanium (III)-citrate [40] as reductant and potassium ferricyanide as oxidant were added via a gas-tight Hamilton syringe. All spectra were normalized to their absorption at 750 nm.

Potentiometric redox titrations

A potentiometric titration of sHdrA monitored by UV-visible spectroscopy was performed inside an anaerobic chamber at 25 °C by oxidizing the as-isolated protein with dichloroindophenol or by reduction with stepwise addition of buffered sodium dithionite, respectively. The protein was used in a concentration of 50 µM with 0.5 µM of a mixture of redox mediators in 200 mM ammonium acetate buffer (pH 6.0) in a total volume of 1.5 mL. The mixture of redox mediators included: dichloroindophenol (+217 mV), trimethylhydroquinone (+115 mV), duroquinone (+50 mV), 1,4-naphthoquinone (+60 mV), indigo disulfonate (−110 mV), safranine (−280 mV), anthraquinone-2-sulfonate (−225 mV), anthraquinone-2,6-disulfonate (−182 mV), neutral red (−325 mV), benzyl viologen (−360 mV) and methyl viologen (−446 mV). Spectra from 250 to 800 nm were measured after attaining equilibrium (15–30 min) at each solution redox potential with an Agilent Technologies (Waldbronn, Germany) 8453E diode array spectrophotometer. All spectra were normalized to their absorption at 750 nm. The reduction potentials were measured with an InLab Redox Micro Ag/AgCl electrode (Mettler-Toledo, Gießen, Germany) calibrated against a saturated quinhydrone solution at pH 7. All values were determined from single determinations and were corrected to potentials versus H_2/H^+ using +207 mV as potential for the Ag/AgCl reference electrode.

EPR spectroscopy and potentiometric redox titrations via EPR

Electron paramagnetic resonance spectra at X-band were obtained using a Bruker EMX spectrometer equipped with an ESR-900 continuous flow of helium cryostat from Oxford Instruments (Abingdon, UK). Spectra were recorded under the following conditions: microwave frequency, 9.39 GHz; microwave power, 2.01 mW; modulation frequency, 100 kHz; modulation amplitude, 1 mT. The EPR-based potentiometric titration was performed inside an anaerobic chamber at 25 °C using 110 µM of HdrA and 180 µM of the same mixture of redox mediators in 100 mM MOPS pH 7.5, 5 mM EDTA. Samples were transferred to EPR tubes under anaerobic conditions, capped, and immediately frozen in liquid nitrogen upon removal from the chamber.

Crystallization and structure determination

Crystallization trials were performed using the sitting-drop method at 18 °C in an anaerobic chamber (Coy Laboratory Products, Grass Lake, MI, USA) with a gas phase of N_2/H_2 (95 : 5 [v/v]) equipped with an OryxNano crystallization robot (Douglas Instruments Ltd., Hungerford, UK). The applied sHdrA solution and the crystallization conditions found with the JBScreen Pentaerythritol (Jena Bioscience) are given in Table 1. Yellow-brownish crystals diffracted to ca. 1.4 Å at the beamline PXII at the Swiss-Light-Source in Villigen (Switzerland). A dataset collected at a wavelength of 1 Å was processed with XDS [62]. A second dataset was measured at the iron edge (1.739 Å) at 2.2 Å resolution (Table 1). The iron positions of the two [4Fe–4S] clusters in the asymmetric unit were identified by SHELXD [63]. Phases were determined by using SHARP [64] and improved by SOLOMON [65]. The model was essentially built automatically by using ARP/wARP [66] and manually completed by using COOT [67]. Refinement was carried out with REFMAC5 [68], PHENIX.REFINE [69] and BUSTER (Phaser; Global Phasing Ltd., Cambridge, UK). The quality of the model was evaluated by COOT and MOLPROBITY [70]. Structure comparison calculations were performed with DALI [71] and surface area calculations by the PISA server [72]. Figures 1, 2A, 3A, and 7 were generated with PYMOL (Schrödinger, LLC, New York, NY, USA). The atomic coordinates and structure factors of sHdrA have been deposited in the Protein Data Bank, www.pdb.org with ID code 6TJR.

Conflicts of interest

The authors declare no conflict of interest.

Author contributions

CD and UE designed the study and wrote the paper. SSV and IACP performed and analyzed EPR spectroscopy. CE, KK, and TK designed experiments. CE, KK, TK, and UD performed experiments. All authors

analyzed the results and approved the final version of the manuscript.

References

1 Rabus R, Venceslau SS, Wohlbrand L, Voordouw G, Wall JD & Pereira IA (2015) A post-genomic view of the ecophysiology, catabolism and biotechnological relevance of sulphate-reducing prokaryotes. *Adv Microb Physiol* **66**, 55–321.

2 Dahl C, Friedrich CG & Kletzin A (2008) Sulfur oxidation in prokaryotes. In Encyclopedia of Life Sciences (ELS). John Wiley & Sons Ltd, Chichester. https://doi.org/10.1002/9780470015902.a0021155

3 Mangold S, Valdés J, Holmes DS & Dopson M (2011) Sulfur metabolism in the extreme acidophile *Acidithiobacillus caldus*. *Front Microbiol* **2**, 17.

4 Frigaard NU & Dahl C (2009) Sulfur metabolism in phototrophic sulfur bacteria. *Adv Microb Physiol* **54**, 103–200.

5 Kletzin A, Urich T, Müller F, Bandeiras TM & Gomes CM (2004) Dissimilatory oxidation and reduction of elemental sulfur in thermophilic archaea. *J Bioenerg Biomembr* **36**, 77–91.

6 Auernik KS & Kelly RM (2010) Physiological versatility of the extremely thermoacidophilic archaeon *Metallosphaera sedula* supported by transcriptomic analysis of heterotrophic, autotrophic, and mixotrophic growth. *Appl Environ Microbiol* **76**, 931–935.

7 Jiang CY, Liu LJ, Guo X, You XY, Liu SJ & Poetsch A (2014) Resolution of carbon metabolism and sulfur-oxidation pathways of *Metallosphaera cuprina* Ar-4 via comparative proteomics. *J Proteom* **109**, 276–289.

8 Liu LJ, Stockdreher Y, Koch T, Sun ST, Fan Z, Josten M, Sahl HG, Wang Q, Luo YM, Liu SJ *et al.* (2014) Thiosulfate transfer mediated by DsrE/TusA homologs from acidothermophilic sulfur-oxidizing archaeon *Metallosphaera cuprina*. *J Biol Chem* **289**, 26949–26959.

9 Stetter KO, Segerer A, Zillig W, Huber G, Fiala G, Huber R & König H (1986) Extremely thermophilic sulfur-metabolizing archaebacteria. *Syst Appl Microbiol* **7**, 393–397.

10 Venceslau SS, Stockdreher Y, Dahl C & Pereira IAC (2014) The "bacterial heterodisulfide" DsrC is a key protein in dissimilatory sulfur metabolism. *Biochim Biophys Acta* **1837**, 1148–1164.

11 Dahl C (2015) Cytoplasmic sulfur trafficking in sulfur-oxidizing prokaryotes. *IUBMB Life* **67**, 268–274.

12 Wagner T, Koch J, Ermler U & Shima S (2017) Methanogenic heterodisulfide reductase (HdrABC-MvhAGD) uses two noncubane [4Fe-4S] clusters for reduction. *Science* **357**, 699–703.

13 Cao X, Koch T, Steffens L, Finkensieper J, Zigann R, Cronan JE & Dahl C (2018) Lipoate-binding proteins and specific lipoate-protein ligases in microbial sulfur

14 Koch T & Dahl C (2018) A novel bacterial sulfur oxidation pathway provides a new link between the cycles of organic and inorganic sulfur compounds. *ISME J* **12**, 2479–2491.

15 Osorio H, Mangold S, Denis Y, Nancucheo I, Esparza M, Johnson DB, Bonnefoy V, Dopson M & Holmes DS (2013) Anaerobic sulfur metabolism coupled to dissimilatory iron reduction in the extremophile *Acidithiobacillus ferrooxidans*. *Appl Environ Microbiol* **79**, 2172–2181.

16 Ouyang J, Liu Q, Li B, Ao J & Chen X (2013) Proteomic analysis of differential protein expression in *Acidithiobacillus ferrooxidans* grown on ferrous iron or elemental sulfur. *Indian J Microbiol* **53**, 56–62.

17 Latorre M, Ehrenfeld N, Cortes MP, Travisany D, Budinich M, Aravena A, Gonzalez M, Bobadilla Fazzini RA, Parada P & Maass A (2016) Global transcriptional responses of *Acidithiobacillus ferrooxidans* Wenelen under different sulfide minerals. *Bioresour Technol* **200**, 29–34.

18 Quatrini R, Appia-Ayme C, Denis Y, Jedlicki E, Holmes DS & Bonnefoy V (2009) Extending the models for iron and sulfur oxidation in the extreme acidophile *Acidithiobacillus ferrooxidans*. *BMC Genom* **10**, 394.

19 Kaster AK, Moll J, Parey K & Thauer RK (2011) Coupling of ferredoxin and heterodisulfide reduction via electron bifurcation in hydrogenotrophic methanogenic archaea. *Proc Natl Acad Sci USA* **108**, 2981–2986.

20 Bennati M, Weiden N, Dinse KP & Hedderich R (2004) ^{57}Fe ENDOR spectroscopy on the iron-sulfur cluster involved in substrate reduction of heterodisulfide reductase. *J Am Chem Soc* **126**, 8378–8379.

21 Thauer RK, Kaster AK, Seedorf H, Buckel W & Hedderich R (2008) Methanogenic archaea: ecologically relevant differences in energy conservation. *Nat Rev Microbiol* **6**, 579–591.

22 Madadi-Kahkesh S, Duin EC, Heim S, Albracht SP, Johnson MK & Hedderich R (2001) A paramagnetic species with unique EPR characteristics in the active site of heterodisulfide reductase from methanogenic archaea. *Eur J Biochem* **268**, 2566–2577.

23 Wischgoll S, Heintz D, Peters F, Erxleben A, Sarnighausen E, Reski R, Van Dorsselaer A & Boll M (2005) Gene clusters involved in anaerobic benzoate degradation of *Geobacter metallireducens*. *Mol Microbiol* **58**, 1238–1252.

24 Mander GJ, Pierik AJ, Huber H & Hedderich R (2004) Two distinct heterodisulfide reductase-like enzymes in the sulfate-reducing archaeon *Archaeoglobus profundus*. *Eur J Biochem* **271**, 1106–1116.

25 Meyerdierks A, Kube M, Kostadinov I, Teeling H, Glöckner FO, Reinhardt R & Amann R (2010)

Metagenome and mRNA expression analyses of anaerobic methanotrophic archaea of the ANME-1 group. *Environ Microbiol* **12**, 422–439.

26 Pereira IAC, Ramos AR, Grein F, Marques MC, da Silva SS & Venceslau SS (2011) A comparative genomic analysis of energy metabolism in sulfate reducing bacteria and archaea. *Front Microbiol* **2**, 69.

27 Nitschke W & Russell MJ (2012) Redox bifurcations: mechanisms and importance to life now, and at its origin: a widespread means of energy conversion in biology unfolds. *BioEssays* **34**, 106–109.

28 Boughanemi S, Lyonnet J, Infossi P, Bauzan M, Kosta A, Lignon S, Giudici-Orticoni MT & Guiral M (2016) Microbial oxidative sulfur metabolism: biochemical evidence of the membrane-bound heterodisulfide reductase-like complex of the bacterium *Aquifex aeolicus*. *FEMS Microbiol Lett* **363**, fnw156.

29 Akhtar MK & Jones PR (2008) Deletion of *iscR* stimulates recombinant clostridial Fe-Fe hydrogenase activity and H_2-accumulation in *Escherichia coli* BL21 (DE3). *Appl Microbiol Biotechnol* **78**, 853–862.

30 Kuchenreuther JM, Grady-Smith CS, Bingham AS, George SJ, Cramer SP & Swartz JR (2010) High-yield expression of heterologous [FeFe] hydrogenases in *Escherichia coli*. *PLoS One* **5**, e15491.

31 Kuriyan J, Krishna TS, Wong L, Guenther B, Pahler A, Williams CH Jr & Model P (1991) Convergent evolution of similar function in two structurally divergent enzymes. *Nature* **352**, 172–174.

32 Schulz GE, Schirmer RH, Sachsenheimer W & Pai EF (1978) The structure of the flavoenzyme glutathione reductase. *Nature* **273**, 120–124.

33 Hernandez HH, Jaquez OA, Hamill MJ, Elliott SJ & Drennan CL (2008) Thioredoxin reductase from *Thermoplasma acidophilum*: a new twist on redox regulation. *Biochemistry* **47**, 9728–9737.

34 Skjoldager N, Blanner Bang M, Rykaer M, Bjornberg O, Davies MJ, Svensson B, Harris P & Hagglund P (2017) The structure of *Lactococcus lactis* thioredoxin reductase reveals molecular features of photo-oxidative damage. *Sci Rep* **7**, 46282.

35 Lennon BW, Williams CH Jr & Ludwig ML (2000) Twists in catalysis: alternating conformations of *Escherichia coli* thioredoxin reductase. *Science* **289**, 1190–1194.

36 Massey V & Palmer G (1966) On the existence of spectrally distinct classes of flavoprotein semiquinones. A new method for the quantitative production of flavoprotein semiquinones. *Biochemistry* **5**, 3181–3189.

37 Evans EW, Dodson CA, Maeda K, Biskup T, Wedge CJ & Timmel CR (2013) Magnetic field effects in flavoproteins and related systems. *Interface Focus* **3**, 20130037.

38 Liu B, Liu H, Zhong D & Lin C (2010) Searching for a photocycle of the cryptochrome photoreceptors. *Curr Opin Plant Biol* **13**, 578–586.

39 O'Reilly JE (1973) Oxidation-reduction potential of the ferro-ferricyanide system in buffer solutions. *Biochim Biophys Acta* **292**, 509–515.

40 Zehnder AJB & Wuhrmann K (1976) Titanium(III) citrate as a nontoxic oxidation-reduction buffering system for culture of obligate anaerobes. *Science* **194**, 1165–1166.

41 Palfey BA & Massey V (1998) Flavin-dependent enzymes. In Comprehensive Biological Catalysis (Sinnott M, ed), pp. 83–154. Academic Press, New York, NY.

42 Mayhew SG (1978) The redox potential of dithionite and SO_2^- from equilibrium reactions with flavodoxins, methyl viologen and hydrogen plus hydrogenase. *Eur J Biochem* **85**, 535–547.

43 Gavrilenko NA, Sukhanow AV & Mokhova OV (2010) Redox and acid–base properties of 2,6-dichlorophenolindophenol immobilized on a polymethacrylate matrix. *J Anal Chem* **65**, 17–20.

44 Roessler MM, Evans RM, Davies RA, Harmer J & Armstrong FA (2012) EPR spectroscopic studies of the Fe-S clusters in the O_2-tolerant [NiFe]-hydrogenase Hyd-1 from *Escherichia coli* and characterization of the unique [4Fe3S] cluster by HYSCORE. *J Am Chem Soc* **134**, 15581–15594.

45 Page CC, Moser CC & Dutton PL (2003) Mechanism for electron transfer within and between proteins. *Curr Opin Chem Biol* **7**, 551–556.

46 Buckel W & Thauer RK (2013) Energy conservation via electron bifurcating ferredoxin reduction and proton/Na^+ translocating ferredoxin oxidation. *Biochim Biophys Acta* **1827**, 94–113.

47 Lubner CE, Jennings DP, Mulder DW, Schut GJ, Zadvornyy OA, Hoben JP, Tokmina-Lukaszewska M, Berry L, Nguyen DM, Lipscomb GL *et al.* (2017) Mechanistic insights into energy conservation by flavin-based electron bifurcation. *Nat Chem Biol* **13**, 655–659.

48 Langen R, Jensen GM, Jacob U, Stephens PJ & Warshel A (1992) Protein control of iron-sulfur cluster redox potentials. *J Biol Chem* **267**, 25625–25627.

49 Brzóska K, Meczynska S & Kruszewski M (2006) Iron-sulfur cluster proteins: electron transfer and beyond. *Acta Biochim Pol* **53**, 685–691.

50 Chen K, Bonagura CA, Tilley GJ, McEvoy JP, Jung YS, Armstrong FA, Stout CD & Burgess BK (2002) Crystal structures of ferredoxin variants exhibiting large changes in [Fe-S] reduction potential. *Nature Struct Biol* **9**, 188–192.

51 Hamill MJ, Chobot SE, Hernandez HH, Drennan CL & Elliott SJ (2008) Direct electrochemical analyses of a thermophilic thioredoxin reductase: interplay between

conformational change and redox chemistry. *Biochemistry* **47**, 9738–9746.

52 O'Donnell ME & Williams CH Jr (1983) Proton stoichiometry in the reduction of the FAD and disulfide of *Escherichia coli* thioredoxin reductase. Evidence for a base at the active site. *J Biol Chem* **258**, 13795–13805.

53 Waterhouse A, Bertoni M, Bienert S, Studer G, Tauriello G, Gumienny R, Heer FT, de Beer TAP, Rempfer C, Bordoli L *et al.* (2018) SWISS-MODEL: homology modelling of protein structures and complexes. *Nucleic Acids Res* **46**, W296–W303.

54 Hamann N, Mander GJ, Shokes JE, Scott RA, Bennati M & Hedderich R (2007) A cysteine-rich CCG domain contains a novel [4Fe-4S] cluster binding motif as deduced from studies with subunit B of heterodisulfide reductase from *Methanothermobacter marburgensis*. *Biochemistry* **46**, 12875–12885.

55 Jensen KP, Ooi BL & Christensen HE (2007) Accurate computation of reduction potentials of 4Fe-4S clusters indicates a carboxylate shift in *Pyrococcus furiosus* ferredoxin. *Inorg Chem* **46**, 8710–8716.

56 Calzolai L, Gorst CM, Zhao ZH, Teng Q, Adams MWW & Lamar GN (1995) ^{1}H NMR investigation of the electronic and molecular structure of the four-iron cluster ferredoxin from the hyperthermophile *Pyrococcus furiosus*. Identification of Asp 14 as a cluster ligand in each of the four redox states. *Biochemistry* **34**, 11373–11384.

57 McLaughlin MI, Lanz ND, Goldman PJ, Lee KH, Booker SJ & Drennan CL (2016) Crystallographic snapshots of sulfur insertion by lipoyl synthase. *Proc Natl Acad Sci USA* **113**, 9446–9450.

58 Tanabe TS, Leimkühler S & Dahl C (2019) The functional diversity of the prokaryotic sulfur carrier protein TusA. *Adv Microb Physiol* **75**, 233–277.

59 Santos AA, Venceslau SS, Grein F, Leavitt WD, Dahl C, Johnston DT & Pereira IA (2015) A protein trisulfide couples dissimilatory sulfate reduction to energy conservation. *Science* **350**, 1541–1545.

60 Fish WW (1988) Rapid colorimetric micromethod for the quantitation of complexed iron in biological samples. *Meth Enzymol* **158**, 357–364.

61 King TE & Morris RO (1966) Determination of acid-labile sulfide and sulhydryl groups. *Meth Enzymol* **10**, 634–637.

62 Kabsch W (2010) XDS. *Acta Crystallogr D Biol Cryst* **66**, 125–132.

63 Schneider TR & Sheldrick GM (2002) Substructure solution with SHELXD. *Acta Crystallogr D Biol Crystallogr* **58**, 1772–1779.

64 de la Fortelle E & Bricogne G (1997) Maximim-likelihood heavy-atom parameter refinement for multiple isomorphous replacement and multiwavelength anomalous diffraction methods. *Meth Enzymol* **276**, 472–494.

65 Abrahams JP & Leslie AG (1996) Methods used in the structure determination of bovine mitochondrial F1 ATPase. *Acta Crystallogr D Biol Cryst* **52**, 30–42.

66 Langer G, Cohen SX, Lamzin VS & Perrakis A (2008) Automated macromolecular model building for X-ray crystallography using ARP/wARP version 7. *Nat Protoc* **3**, 1171–1179.

67 Emsley P & Cowtan K (2004) Coot: model-building tools for molecular graphics. *Acta Crystallogr D Biol Cryst* **60**, 2126–2132.

68 Murshudov GN, Vagin AA & Dodson EJ (1997) Refinement of macromolecular structures by the maximum-likelihood method. *Acta Crystallogr D Biol Cryst* **53**, 240–255.

69 Afonine PV, Grosse-Kunstleve RW, Chen VB, Headd JJ, Moriarty NW, Richardson JS, Richardson DC, Urzhumtsev A, Zwart PH & Adams PD (2010) phenix.model_vs_data: a high-level tool for the calculation of crystallographic model and data statistics. *J Appl Crystallogr* **43**, 669–676.

70 Davis IW, Leaver-Fay A, Chen VB, Block JN, Kapral GJ, Wang X, Murray LW, Arendall WB 3rd, Snoeyink J, Richardson JS & *et al.* (2007) MolProbity: all-atom contacts and structure validation for proteins and nucleic acids. *Nucleic Acids Res* **35**, W375–W383.

71 Holm L & Laakso LM (2016) Dali server update. *Nucleic Acids Res* **44**, W351–W355.

72 Krissinel E & Henrick K (2007) Inference of macromolecular assemblies from crystalline state. *J Mol Biol* **372**, 774–797.

73 Riederer BM (2009) Oxidation proteomics: the role of thiol modifications. *Curr Proteomics* **6**, 51–62.

74 Everett SA, Folkes LK, Wardman P & Asmus KD (1994) Free radical repair by a novel perthiol - Reversible hydrogen-transfer and perthiyl radical formation. *Free Radic Res* **20**, 387–400.

75 Nagy P & Ashby MT (2007) Reactive sulfur species: Kinetics and mechanisms of the oxidation of cysteine by hypohalous acid to give cysteine sulfenic acid. *J Am Chem Soc* **129**, 14082–14091.

76 Enami S, Hoffmann MR & Colussi AJ (2009) Simultaneous detection of cysteine sulfenate, sulfinate, and sulfonate during cysteine interfacial ozonolysis. *J Phys Chem B* **113**, 9356–9358.

77 Nagy P & Winterbourn CC (2010) Redox chemistry of biological thiols. *Adv Mol Toxicol* **4**, 183–222.